Testing the Limits of the Single Particle Model in ^{16}O(e, e′p): An Update to E89-003

A. Saha [1]

Thomas Jefferson National Accelerator Facility, Newport News, VA 23606, USA

W. Bertozzi

Massachusetts Institute of Technology, Cambridge, MA 02139, USA

L. B. Weinstein

Old Dominion University, Norfolk, VA 23529, USA

K. G. Fissum

University of Lund, Box 118, SE-221 00 Lund, Sweden

and the Jefferson Lab Hall A Collaboration

We propose to measure the cross section, R_{lt}, and A_{lt} for the ^{16}O$(e, e'p)$ reaction with higher precision and to much higher missing momentum and missing energy than in E89-003. We will perform this measurement at the same energy and momentum transfer ($Q^2 = 0.8$ (GeV/c)^2 and $\omega = 0.445$ GeV). This experiment will take advantage of the Hall A high-precision spectrometers and the self-normalizing waterfall target; accurate, modern, relativistic $(e, e'p)$ theory; and observables sensitive to specific physical parameters. We will compare our results to theoretical predictions in order to determine:

(i) the limits of validity of the single-particle model of valence proton knockout;

(ii) the effects of relativity and spinor distortion on valence proton knockout using the diffractive character of the A_{lt} asymmetry;

(iii) the bound-state wave function and spectroscopic factors for valence knockout; and

(iv) the longitudinal component of the higher missing energy (two-nucleon knockout) cross section (through the R_{lt} response function), including the predicted two-nucleon knockout correlation ridge.

To compensate for the lower cross sections at higher missing momenta, we will increase the beam energy and the luminosity over those used for E89-003. This proposal is an update to E89-003, which has time remaining. We are requesting 31 days of beamtime to perform these measurements.

1 Introduction

Exclusive and semi-exclusive quasielastic proton knockout reactions, $(e, e'p)$, have been very successful in the study of both nuclear structure and reaction mechanisms. In general, but not without exceptions, the single-particle aspect of nuclear structure was studied using proton removal from valence states, while other aspects of the structure as well as the reaction mechanism were studied at higher missing energies. Unfortunately, no coherent theoretical picture exists that describes data in these two excitation regions, and the theoretical tools used to describe these two regions are different. Hence, in our present understanding, these two regions are related mainly by the transfer of strength from the valence states to higher missing energies [1]. Experimentally, it is convenient to perform measurements simultaneously in these two excitation regions.

The response functions which make up the cross section provide independent observables which are selectively sensitive to various aspects of the nuclear current. Hence, in addition to measuring cross sections, the extraction of these additional observables is important in forming a complete picture of the structure and the reactions.

^{16}O has long been a favorite nucleus for theorists, being a doubly closed-shell nucleus whose structure is easier to model than other nuclei. Experimentally, it has been studied extensively. However, it is not as convenient a target as ^{12}C for example, and hence less experimental data are available from $^{16}\mathrm{O}(e, e'p)$ reactions. Fortunately, the Hall A waterfall target [2] is a convenient and self-normalizing ^{16}O target.

The knockout of $1p$-shell protons in $^{16}\mathrm{O}(e, e'p)$ was studied by Bernheim *et al.* [3] and Chinitz *et al.* [4] at Saclay, Spaltro *et al.* [5] and Leuschner *et al.* [6] at NIKHEF, and Blomqvist *et al.* [7] at Mainz at four-momentum transfers $Q^2 < 0.4$ (GeV/c)^2. In these experiments, the cross sections were measured as a function of missing momentum p_{miss}, and spectroscopic factors were extracted. These published spectroscopic factors range between 0.5 and 0.7, but Kelly showed [8] that the Mainz data [7] suggest a significantly smaller normalization factor. Chinitz *et al.* [4] and Spaltro *et al.* [5] also extracted the longitudinal-transverse interference response, R_{lt}, at both $Q^2 = 0.3$ (GeV/c)^2 and 0.2 (GeV/c)^2 respectively. Their extracted R_{lt} for the $1p_{1/2}$-state agree, but those for the $1p_{3/2}$-state disagree dramatically (see Fig. 1). DWIA calculations by Kelly [9] based on fits to distorted momentum distributions measured in parallel kinematics at NIKHEF [6] are consistent with the data of Chinitz *et al.* [4]. The same calculations nicely describe more recent data at $Q^2 = 0.8$

[1] contact person: email saha@jlab.org; telephone +1 (757) 269-7605

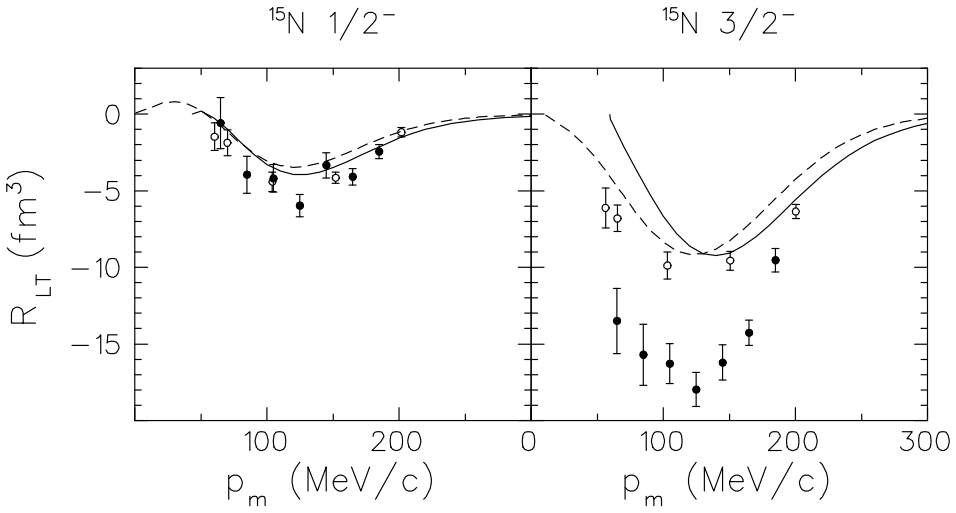

Fig. 1. Longitudinal-transverse interference responses as a function of missing momentum for the $1p$-shell of ^{16}O. Open (filled) circles were extracted from quasielastic data obtained by Chinitz *et al.* [4] (Spaltro *et al.* [5]) at $Q^2 = 0.3$ (GeV/c)^2 ($Q^2 = 0.2$ (GeV/c)^2). The calculations [9] are based on fits to distorted momentum distributions measured in parallel kinematics by Leuschner *et al.* [6]. Figure courtesy J. J. Kelly.

(GeV/c)^2 [10] which are outlined below.

Not many data are available for ^{16}O$(e, e'p)$ at higher missing energies, and much of what we know about this excitation region is from studies of other nuclei, mainly from ^{12}C. Above the two-nucleon emission threshold, excess transverse strength is observed for many nuclei [11–14]. This phenomenon persists over a large range of four-momentum transfers, though the excess transverse strength at small $p_{\rm miss}$ seems to decrease with increasing Q^2 [14]. Several theoretical attempts to explain the data at high missing energies using two-body knockout models [15–17] and tensor and short-range correlations [1] fail. Even for quasielastic kinematics, high missing energy cross sections are associated with significant contributions from non-single-particle processes.

1.1 Results from E89-003

More recently, the Hall A Collaboration has used the ^{16}O$(e, e'p)$ reaction to study nucleon removal from the valence $1p$-shell [10] as well as from the $1s_{1/2}$-state and higher residual excitations [18]. This was the first part of JLab experiment E89-003 [19] which was the first experiment performed in Hall A. All measurements were made at a fixed four-momentum transfer, $Q^2 = 0.8$ (GeV/c)^2, and in quasielastic kinematics at $\omega = 0.445$ GeV. Cross sections and response functions were measured as a function of missing energy at several different missing momenta up to $p_{\rm miss} = 345$ MeV/c.

One of the most striking results is the contrast between the success of theoretical calculations to describe the measured observables in the $1p$-shell removal and the failure of the same calculations to describe the observables related to the $1s_{1/2}$-state removal and higher residual excitations. It is clear that even up to a missing momentum of about 345 MeV/c, the single-particle aspect of the $1p$-shell structure is dominant, whereas for the $1s_{1/2}$-state and for higher missing energies, other aspects of the wave function (such as two-nucleon correlations) and/or of the reaction mechanism (two-nucleon currents such as Meson Exchange Currents (MEC) or Isobar Configurations (IC)) mask the single-particle picture. These other aspects become more prominent with increasing missing momenta.

1.1.1 Valence 1p-shell knockout

The five-fold differential cross section was measured in perpendicular kinematics for proton removal from the $1p_{1/2}$- and $1p_{3/2}$-states at eight $p_{\rm miss}$ values in the range $-345 < p_{\rm miss} < +345$ MeV/c (see Fig. 2). Note that the angle between the ejected proton and the virtual photon is θ_{pq}, and the azimuthal angle is ϕ. We take $\theta_{pq} > 0$ to correspond to $\phi = 180°$, $\theta_p > \theta_q$, and $p_{\rm miss} > 0$.

The cross section is well-described by fully relativistic DWIA calculations [20] which solve the Dirac equation and include Dirac spinor distortions of both the bound and scattered states. It is also well-described by relativistic DWIA calculations which solve a relativized Schrödinger equation and use the Effective Momentum Approximation (EMA) to include the lower components of the Dirac spinors [9]. However, the EMA breaks down at $p_{\rm miss} > 275$ MeV/c, and hence the latter calculations are less successful in reproducing the data in this $p_{\rm miss}$ range. Both calculations use the NLSH [21] bound-state wave function (bswf) which yields values for the binding and single-particle energies (as well as a charge radius for ^{16}O) which are in good agreement with data. The spectroscopic factors extracted for the $1p_{1/2}$- ($1p_{3/2}$-) states were 0.73 (0.71) and 0.72 (0.67) for the Udias and Kelly calculations respectively. The spectroscopic factors extracted by Udias are consistent with those he extracted from the data of Chinitz [4], Spaltro [5], and Leuschner [6] at lower four-momentum transfers, but only when taking into account the large uncertainties in those obtained at lower Q^2 (most notably [6]). We note this constant behavior in light of recent suggestions by Lapikas *et al.* [22] that spectroscopic factors for the $1p$-state of ^{12}C may be momentum-transfer dependent.

The $R_l + (v_{tt}/v_l)R_{tt}$, R_t, and R_{lt} response functions (see Fig. 3) as well as the left-right asymmetry, A_{lt} (see Fig. 4), were also extracted for the $1p$-shell proton knockout and compared to the relativistic DWIA calculations.

The calculations are in good agreement with the measured quantities. The

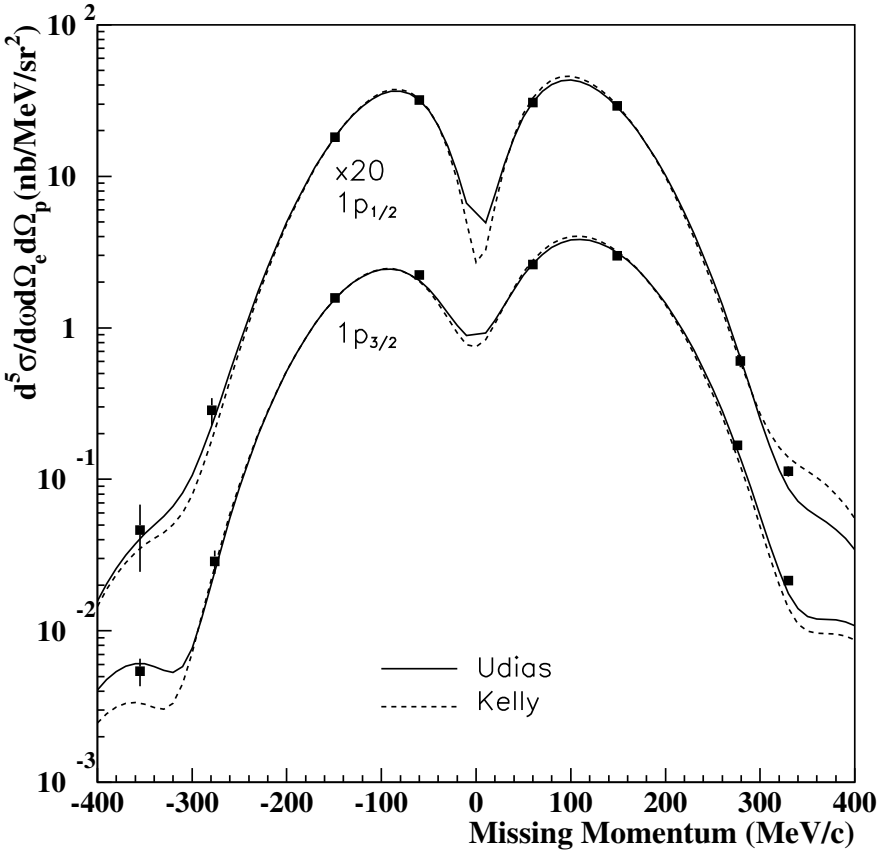

Fig. 2. Five-fold differential cross sections obtained in perpendicular kinematics for the knockout of $1p$-shell protons from ^{16}O as a function of missing momentum. Details pertaining to the calculation represented by the solid (dashed) line may be found in [20] ([9]). Figure courtesy J. Gao.

most striking result is a structure in A_{lt} which is predicted and well-reproduced by the calculations only when spinor distortions are fully included (see Fig. 4). While A_{lt} is very sensitive to this dynamic enhancement of the lower components of the Dirac spinors, especially at $p_{\rm miss} > 275$ MeV/c, the inclusion of these spinor distortions is also needed to reproduce R_{lt} at $p_{\rm miss} < 275$ MeV/c. Note that, although striking, this conclusion is drawn from only a small number of data points and needs to be confirmed.

It should be emphasized that neither DWIA calculation includes contributions from two-body effects such as MEC, IC, or from initial-state correlations. Hence, it was concluded that up to a $p_{\rm miss}$ of 345 MeV/c, well above the Fermi-momentum, these effects are not important.

It is important, then, to push measurements to higher $p_{\rm miss}$, into the region where A_{lt} is increasingly sensitive to dynamical relativistic effects (see the

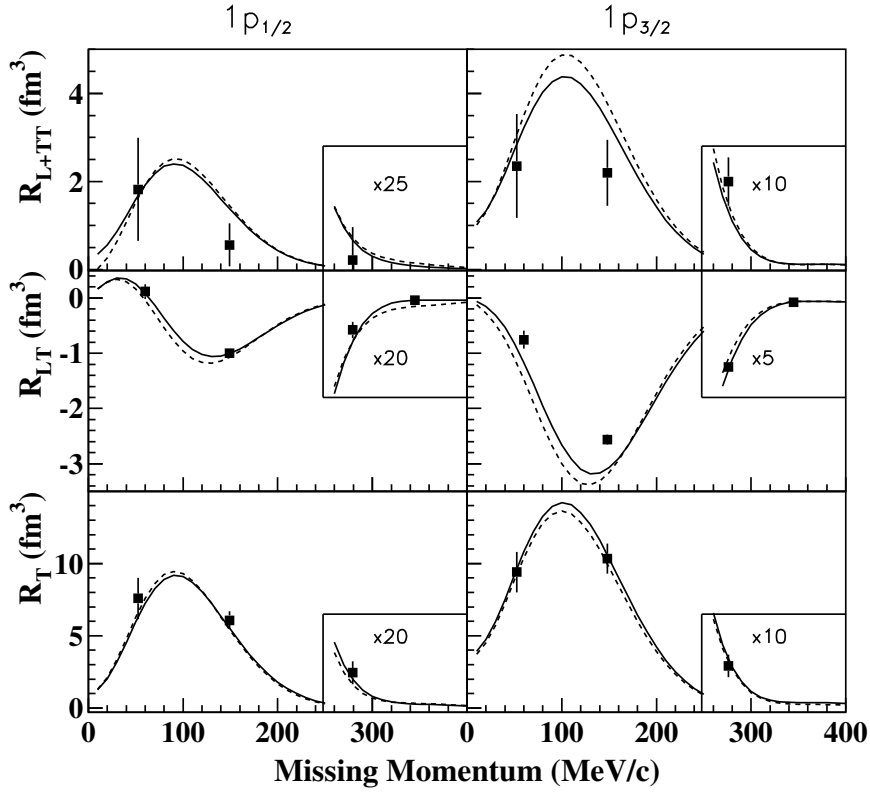

Fig. 3. Measured $R_l + (v_{tt}/v_l)R_{tt}$ (abbreviated R_{l+tt}), R_t, R_{lt}, and DWIA calculations as a function of missing momentum. Total error bars are shown. The solid (dashed) line is the Udias [20] (Kelly [9]) calculation. Figure courtesy J. Gao.

bottom panels of Figs. 9 and 10), and also where two-body effects should become important. In this respect, it is noteworthy that Udias *et al.* may be able to include the effects of initial-state correlations and of MEC in the foreseeable future [23].

The results for the $1p$-shell as well as comparison to theory are described in detail in the manuscript attached as Appendix 1 [10], which has recently been published in *Physical Review Letters*.

1.1.2 Higher missing energy

The $^{16}\mathrm{O}(e,e'p)$ reaction was also studied at higher missing energies [18]. Missing energy spectra for up to $E_{\mathrm{miss}} = 120$ MeV were measured for four missing momenta in the range 50 - 345 MeV/c. Also measured were the R_l and R_t responses for $p_{\mathrm{miss}} \approx 60$ MeV/c, and the $R_l + (v_{tt}/v_l)R_{tt}$, R_t, and R_{lt} responses

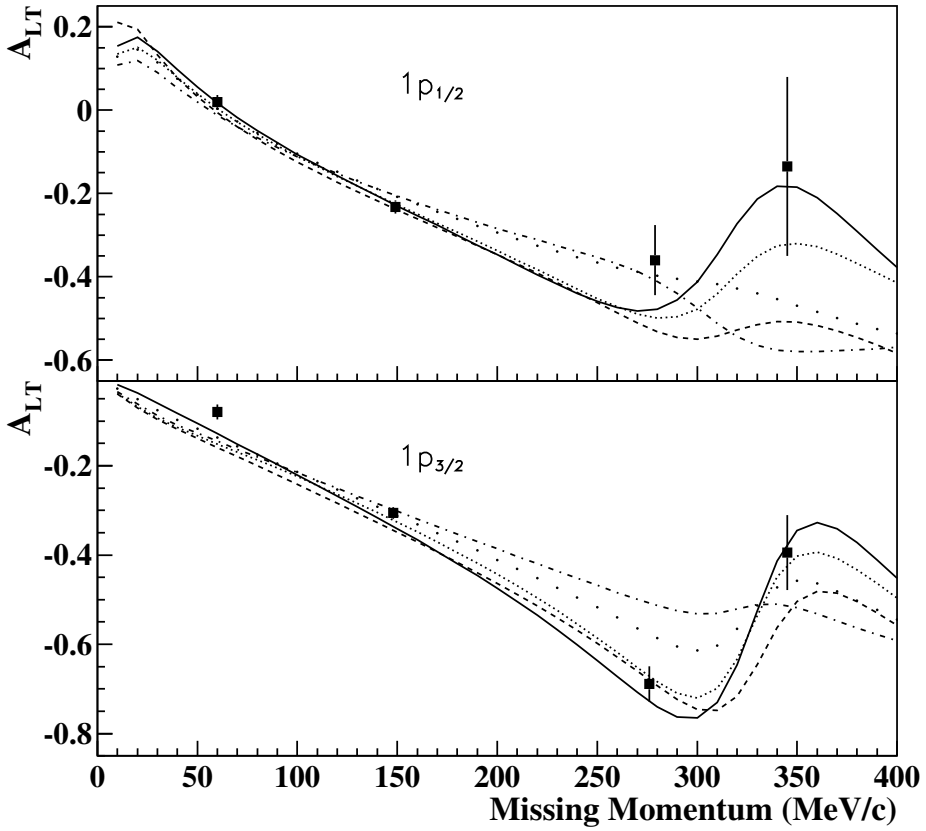

Fig. 4. The measured left-right asymmetry A_{lt} in comparison to DWIA calculations as a function of missing momentum. Total error bars are shown. The dashed line is the Kelly [9] calculation, while all others have been provided by Udias [20]. In particular, the solid line is a fully relativistic calculation, while the densely (loosely) dotted line has only the bound- (scattered-) state spinor distortion included. The dotted-dashed line does not include any spinor distortions, making it essentially identical to factorized calculations. Figure courtesy J. Gao.

for $p_{\rm miss} = 145$ MeV/c and 280 MeV/c. The main feature of this measurement is the clear manifestation of the $1s_{1/2}$-state at $p_{\rm miss} \approx 50$ - 60 MeV/c, and its decreasing prominence with increasing $p_{\rm miss}$. The $1s_{1/2}$-state is clearly visible in the $E_{\rm miss}$ spectrum at $p_{\rm miss} = 50$ MeV/c, and in the response functions at $p_{\rm miss} = 60$ MeV/c (see Figs. 6 and 7).

The measured observables were compared to the same DWIA calculations [9,23] that successfully predicted the $1p$-shell removal data. As previously mentioned, these calculations are based on a single-particle picture and hence assume the dominance of $1s_{1/2}$-state knockout in the region $20 < E_{\rm miss} < 60$ MeV. The data were also compared to calculations by Ryckebusch *et al.*

[16,24–27] which include a single-particle non-relativistic Hartree-Fock (HF) component which uses the same potential for the bound state and the ejectile nucleon. Ryckebusch also calculated the contributions from both $(e, e'pp)$ and $(e, e'pn)$ due to pion-exchange currents, intermediate $\Delta(1232)$ creation, central short-range correlations, and tensor correlations (see Fig. 5).

These observables are also well-described by all calculations [9,23,27] with reasonable occupancy in the calculation of Kelly of 0.73. However, at higher $p_{\rm miss}$, the $1s_{1/2}$-state peak is increasingly masked by strength at higher and lower missing energies, and for $p_{\rm miss} > 280$ MeV/c, the missing energy spectrum is flat with a constant cross section of a few pb/(MeV/c)^2/sr^2 all the way up to the highest measured missing energy of 120 MeV. The $1s_{1/2}$-state peak is decreasingly noticeable with increasing $p_{\rm miss}$ in the measured response functions as well (see Figs. 7 and 8).

Similarly, the calculations increasingly fail to reproduce the measured $1s_{1/2}$-state observables with increasing $p_{\rm miss}$. It should be noted that the HF calculations of Ryckebusch *et al.* are able to qualitatively reproduce the strength of the $1s_{1/2}$-state for the entire $p_{\rm miss}$ range. However, this is due to the non-absorptive potential used which yields strength at $p_{\rm miss} > 250$ MeV/c that is an order of magnitude larger than that of the DWIA calculations. As a result, the HF calculations overpredict the cross section of the $1p$-shell by the same amount for $p_{\rm miss} > 250$ MeV, and are unreliable for that $p_{\rm miss}$ range. Hence, neither the DWIA nor the HF calculations are able to reliably reproduce the $1s_{1/2}$-state behavior because at large $p_{\rm miss}$, the single-particle aspect of proton removal is increasingly masked by other processes or components of the wave function.

For missing energies higher than the $1s_{1/2}$-state, the measured cross section, including the flat region beginning at $p_{\rm miss} = 250$ MeV/c, is described (to within a factor of two) in the calculations of Ryckebusch *et al.* by contributions from $(e, e'pp)$ and $(e, e'pn)$ arising from two-body currents and from central and tensor short-range correlations. Measurements of additional observables are needed to verify these contributions (see Fig. 5).

The results for the $1s_{1/2}$-state and higher missing energies as well as comparison to theory are described in detail in the draft manuscript attached as Appendix 2 [18], which is to be submitted to *Physical Review Letters* in the very near future.

1.1.3 Summary

To summarize the results from the first phase of our ^{16}O$(e, e'p)$ measurement, $1p$-shell proton knockout appears to be extraordinarily well-described up to $p_{\rm miss} = 345$ MeV/c by a fully relativistic, single-nucleon knockout DWIA cal-

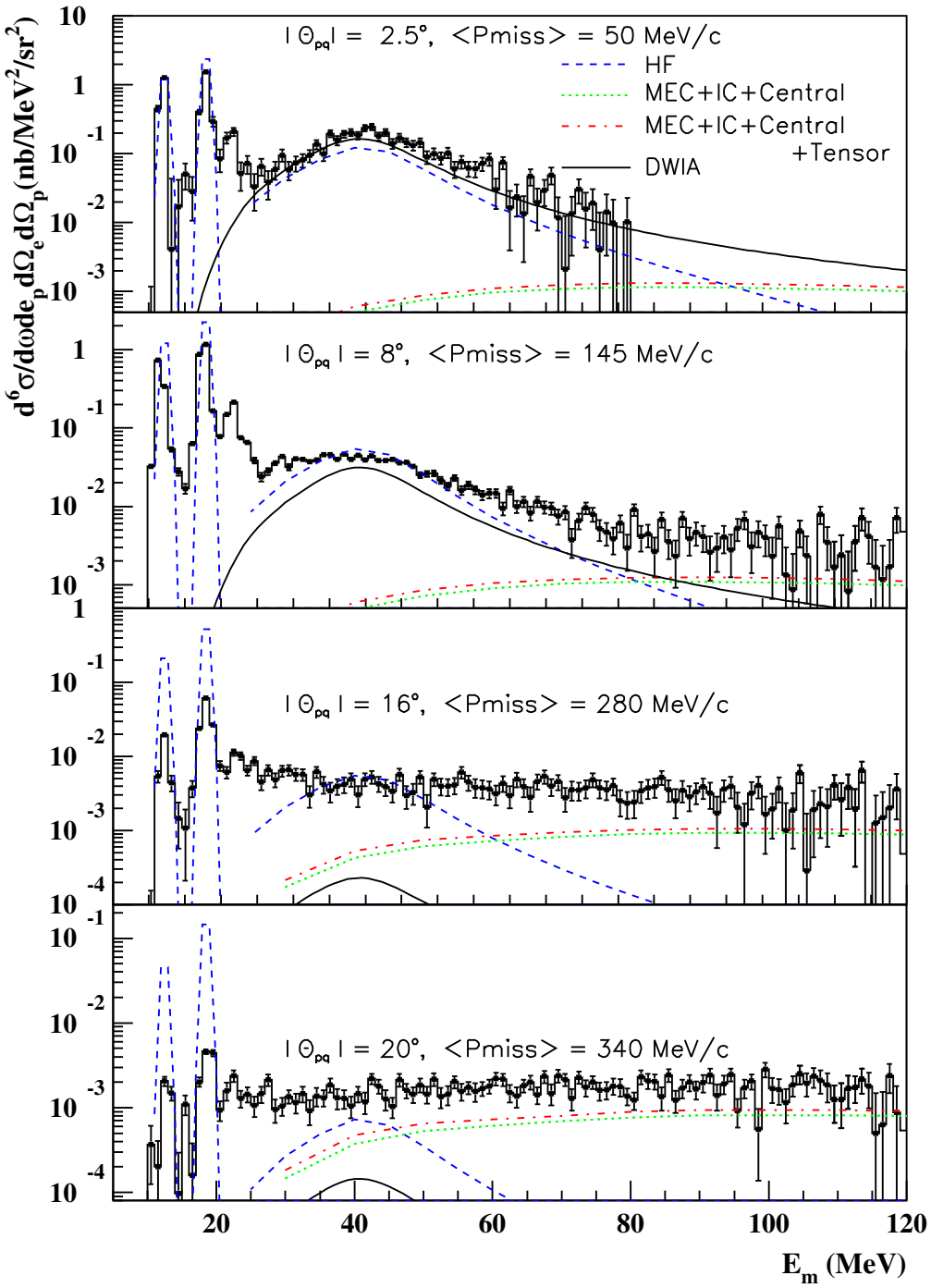

Fig. 5. Six-fold differential ^{16}O$(e,e'p)$ cross sections as a function of missing energy for four different average values of missing momentum. The solid (dashed) lines represent the Kelly [9] (Ryckebusch *et al.* [16,24–27]) single nucleon knockout calculations folded with the Lorentzian parametrization of Mahaux [28]. The dotted Ryckebusch *et al.* calculation shows the $(e,e'pp)$ and $(e,e'pn)$ contributions due to pion-exchange currents, intermediate $\Delta(1232)$ creation, and central short-range correlations, while the dot-dashed calculation also includes tensor correlations. The prominence of the broad peak centered at $E_{\rm miss} \approx 40$ MeV, which is primarily due to knockout from the $1s_{1/2}$-state, decreases with increasing $p_{\rm miss}$. Figure courtesy N. Liyanage.

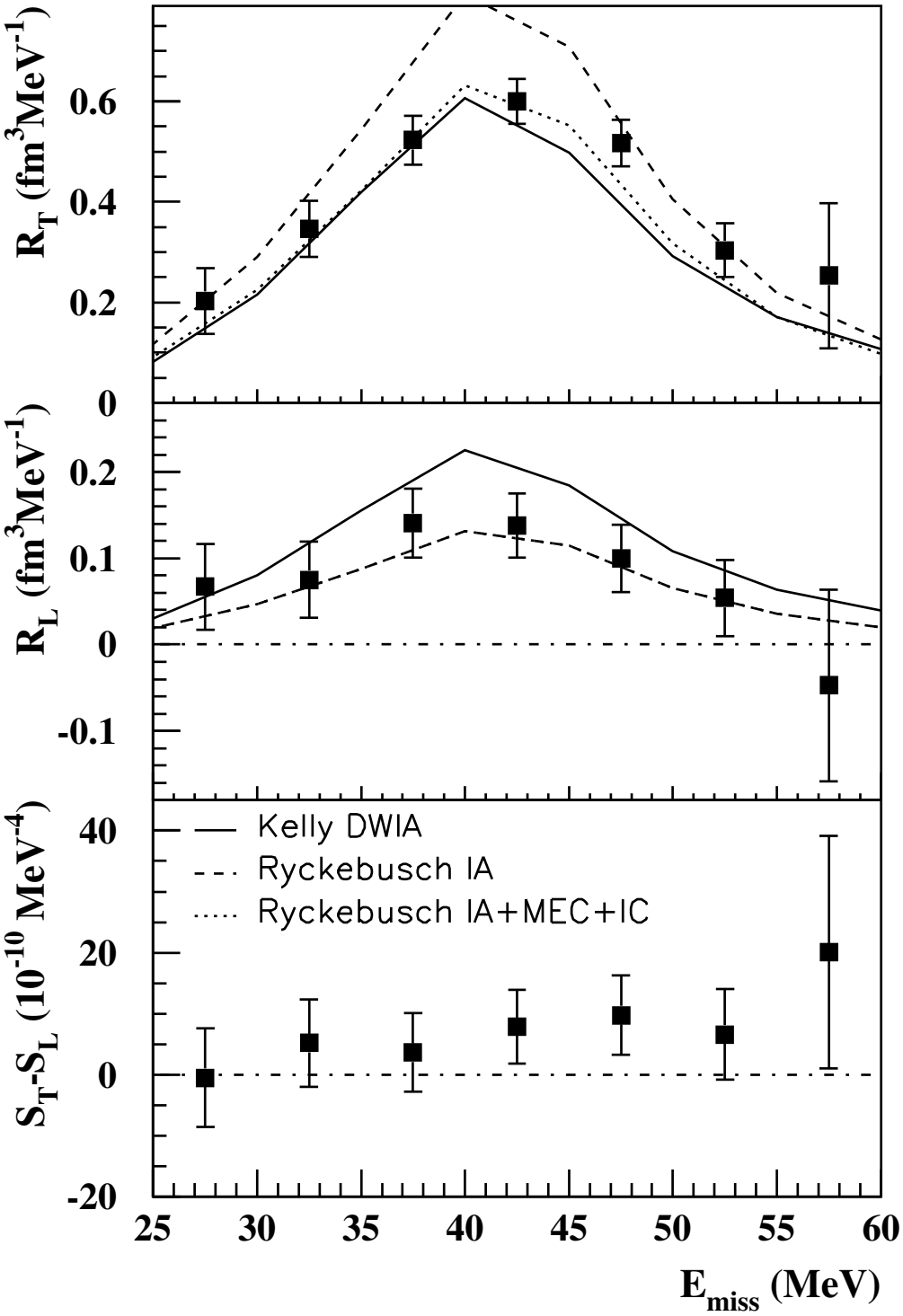

Fig. 6. The separated transverse and longitudinal response functions and the difference between the transverse and longitudinal spectral functions at $p_{\rm miss} \approx 60$ MeV/c as a function of missing energy. The solid (dashed) lines represent the Kelly [9] (Ryckebusch *et al.* [16,24–27]) calculations, which have been binned in the same manner as the data. The broad peak in both R_t and R_l centered at $E_{\rm miss} \approx 40$ MeV is primarily due to single-particle knockout from the $1s_{1/2}$-state. Figure courtesy N. Liyanage.

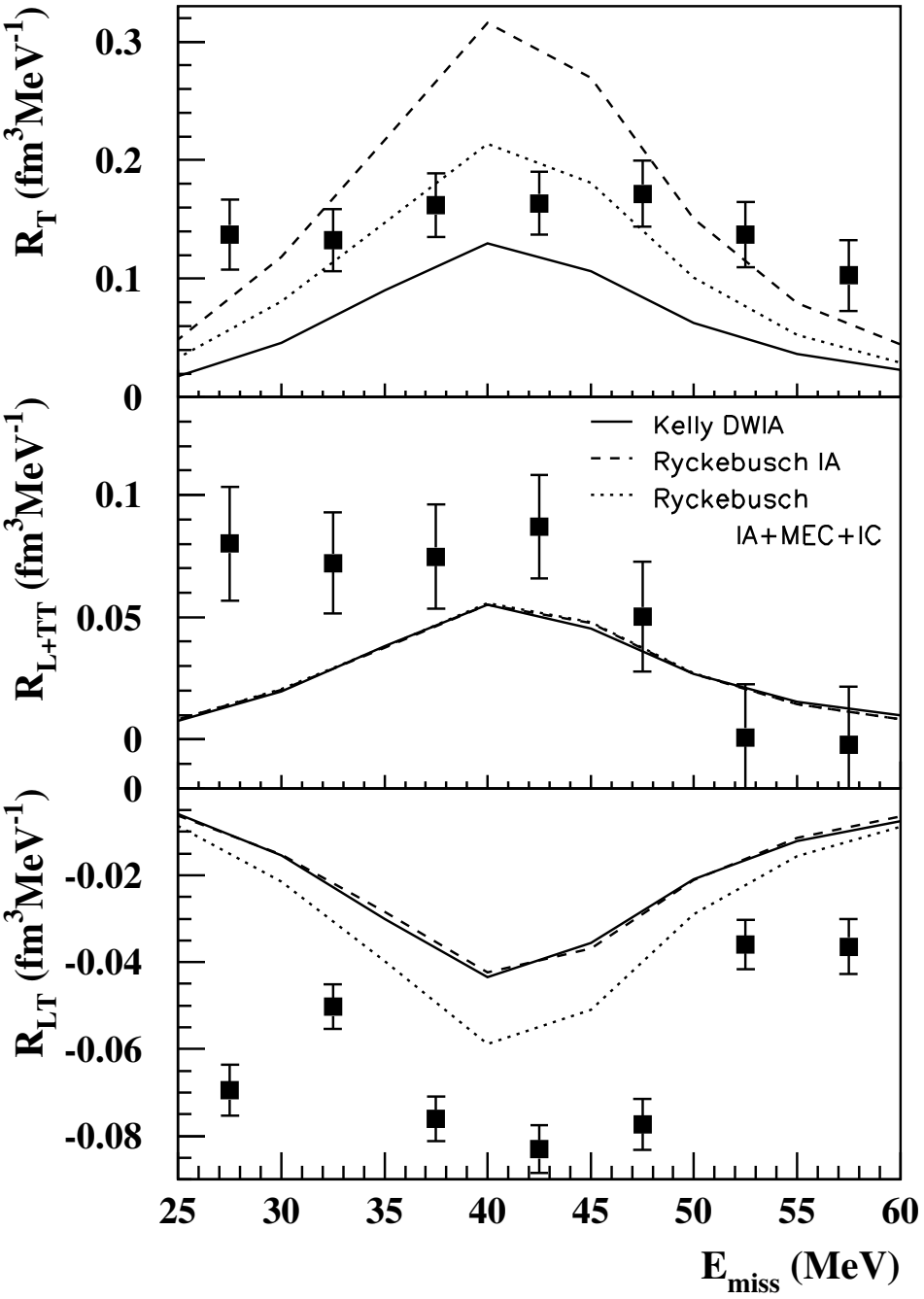

Fig. 7. The separated R_t, $R_l + (v_{tt}/v_l)R_{tt}$ (abbreviated R_{l+tt}), and R_{lt} response functions at $p_{\rm miss} \approx 145$ MeV/c as a function of missing energy. The solid (dashed) lines represent the Kelly [9] (Ryckebusch *et al.* [16,24–27]) calculations, which have been binned in the same manner as the data. Figure courtesy N. Liyanage.

culation that includes the effects of spinor distortions. However, this is not true for $E_{\rm miss} > 25$ MeV. In this case, the reaction is well-described by single-nucleon knockout calculations only at low missing momentum ($p_{\rm miss} < 100$ MeV/c). At higher missing momenta, the single particle aspects are increasingly masked by more complicated states and processes.

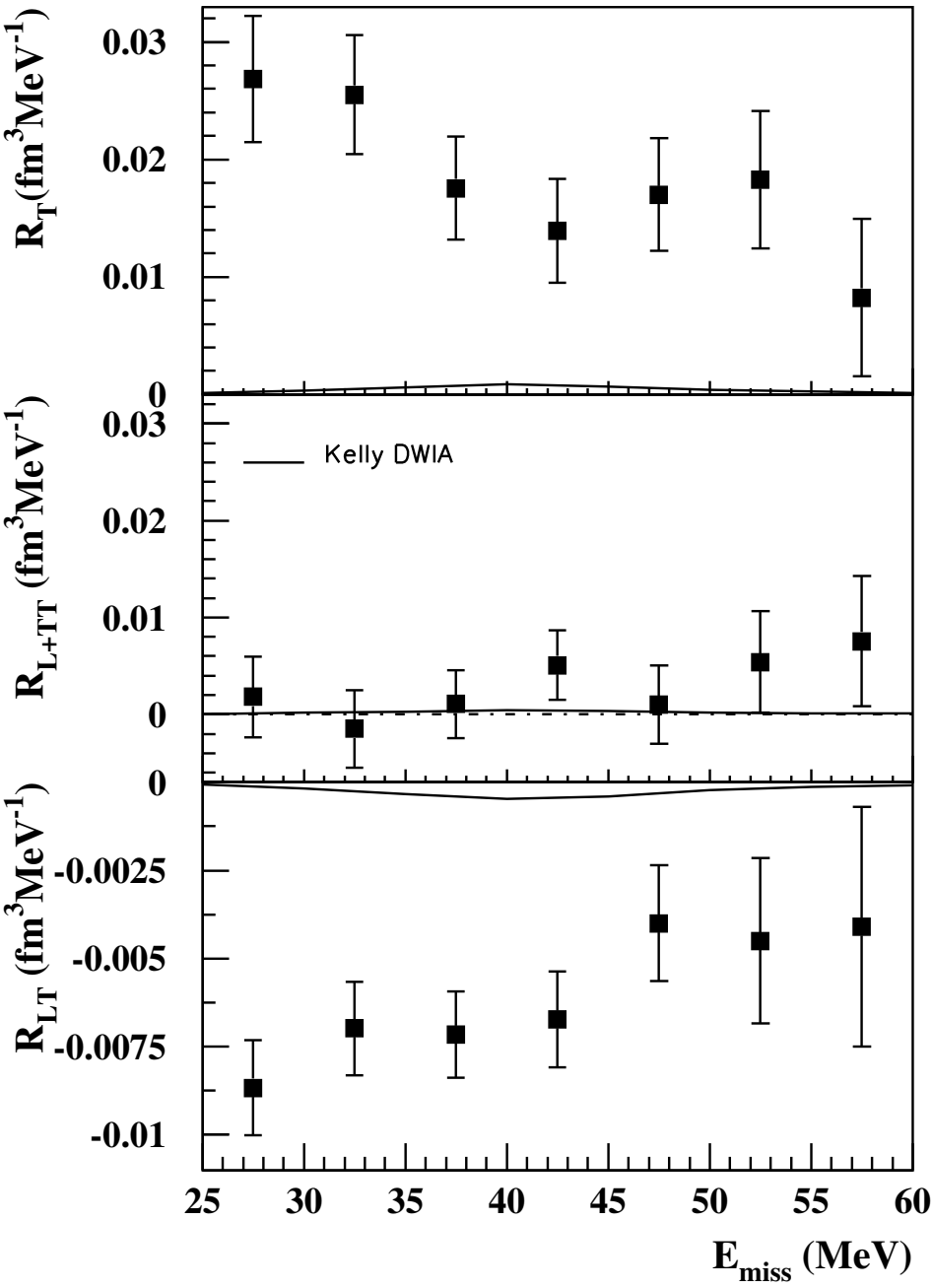

Fig. 8. The separated R_t, $R_l + (v_{tt}/v_l)R_{tt}$ (abbreviated R_{l+tt}), and R_{lt} response functions at $p_{\rm miss} \approx 280$ MeV/c as a function of missing energy. The solid (dashed) lines represent the Kelly [9] (Ryckebusch *et al.* [16,24–27]) calculations, which have been binned in the same manner as the data. Figure courtesy N. Liyanage.

2 Proposed measurement

We propose to measure the cross section, R_{lt}, and A_{lt} for the ^{16}O$(e, e'p)$ reaction with higher precision and to much higher missing momentum and missing energy than in E89-003. We plan to take advantage of three crucial ingredients:

(i) the high-precision Hall A experimental equipment;
(ii) a tested, high-precision, fully relativistic calculation; and
(iii) observables sensitive to specific physical parameters.

We will compare our results to the theoretical predictions in order to determine:

(i) the limits of validity of the single-particle model of valence proton knockout;
(ii) the effects of relativity and spinor distortion on valence proton knockout using the diffractive character of the A_{lt} asymmetry;
(iii) the bound-state wave function and spectroscopic factors for valence knockout;
(iv) the longitudinal component of the higher missing energy (two-nucleon knockout) cross section (through the R_{lt} response function); and
(v) the longitudinal component of the predicted two-nucleon knockout correlation ridge (also through R_{lt}).

To compensate for the smaller cross sections at higher missing momenta, we will raise the beam energy to 4.045 GeV (increasing $\sigma_{\rm Mott}$ by a factor of 2.3) and increase the luminosity by a factor of 2.8. We will also save time by not performing Rosenbluth separations. Instead, we will focus on A_{lt} and R_{lt}. For the valence knockout, these observables are particularly sensitive to dynamical relativistic effects in the wavefunction and the current operator. At higher missing energies, we will use the dominant transverse amplitude to magnify the much smaller longitudinal amplitude. This will show us significant changes in the longitudinal amplitude, for example at the predicted two-nucleon correlation ridge.

We propose to use a single momentum and energy transfer, $Q^2 = 0.8$ (GeV/c)^2 and $\omega = 0.445$ GeV, the same as that used for E89-003. This will enable us to greatly enhance the data base available for this momentum transfer. We will use a single electron kinematics ($E_{beam} = 4.045$ GeV, $\theta_e = 13.48^o$) which will let us use the static HRS$_e$ as a continuous luminosity monitor. We will vary the missing momentum by moving the HRS$_h$, and the missing energy by changing the field in the HRS$_h$. The target will be similar to the three-foil waterfall target used in E89-003 [2], but the flow rate will be doubled to provide a thickness of about 290 mg/cm^2 per foil along the beamline. As in E89-003, electron scattering from the ^{1}H in the water molecule will be used for the experimental determination of the magnitude and direction of the three-momentum transfer, and for absolute normalization. Based on the cumulative experience of the Hall A Collaboration, we expect to attain systematic uncertainties of 3%.

Table 1 presents the proposed kinematics in detail. We refer to Figs. 9 and 10 for the anticipated 1p-shell data, including expected error bars.

label	p(HRS$_h$) (GeV/c)	θ_{pq} (°)	θ_h (°)	$< p_{\rm miss} >$ (GeV/c)	$< E_{\rm miss} >$ (GeV)
A1	0.987	-30.0	27.02	-0.515	0.012
B1	0.991	-25.0	32.02	-0.431	0.012
C1	0.994	-20.0	37.02	-0.346	0.012
C2	0.919	-20.0	37.02	-0.343	0.065
C3	0.844	-20.0	37.02	-0.355	0.116
D1	0.996	-16.0	41.02	-0.278	0.012
E1	0.998	-12.0	45.02	-0.209	0.012
E2	0.923	-12.0	45.02	-0.215	0.065
E3	0.848	-12.0	45.02	-0.246	0.116
F1	0.999	-8.0	49.02	-0.140	0.012
F2	0.924	-8.0	49.02	-0.155	0.065
F3	0.849	-8.0	49.02	-0.199	0.116
G1	0.999	-6.0	51.02	-0.105	0.012
H1	1.000	-4.0	53.02	-0.070	0.012
H2	0.925	-4.0	53.02	-0.101	0.065
H3	0.850	-4.0	53.02	-0.163	0.116
I1	1.000	+4.0	61.02	+0.070	0.012
I2	0.925	+4.0	61.02	+0.101	0.065
I3	0.850	+4.0	61.02	+0.163	0.116
J1	0.999	+6.0	63.02	+0.105	0.012
K1	0.999	+8.0	65.02	+0.140	0.012
K2	0.924	+8.0	65.02	+0.155	0.065
K3	0.849	+8.0	65.02	+0.199	0.116
L1	0.998	+12.0	69.02	+0.209	0.012
L2	0.923	+12.0	69.02	+0.215	0.065
L3	0.848	+12.0	69.02	+0.246	0.116
M1	0.996	+16.0	73.02	+0.278	0.012
N1	0.994	+20.0	77.02	+0.346	0.012
N2	0.919	+20.0	77.02	+0.343	0.065
N3	0.844	+20.0	77.02	+0.355	0.116
O1	0.991	+25.0	82.02	+0.431	0.012
P1	0.987	+30.0	87.02	+0.515	0.012
Q1	0.979	+38.0	95.02	+0.644	0.012
R1	0.972	+45.0	102.02	+0.755	0.012

Table 1
The proposed kinematics. The central electron kinematics are fixed at $E_0 = 4.045$ GeV, $E_f = 3.600$ GeV, and $\theta_e = 13.48°$, resulting in $q = 1.000$ GeV/c at $\theta_q = 57.02°$. The numbers 1-3 in the labels correspond to different momentum bites for the HRS$_h$ at fixed θ_h (see 3.2.2).

We have different, although linked, physics goals for the valence knockout and for higher missing energies. For $1p$-shell knockout at low missing momentum ($p_{\rm miss} < 200$ MeV/c), we propose to measure the cross section as a function of missing momentum (distorted momentum distributions) in order to constrain the bswf and to accurately determine the spectroscopic factors. We will also measure R_{lt} and A_{lt} up to $p_{\rm miss} \approx 500$ MeV/c in order to further test the relativistic DWIA calculations which predict great sensitivity to relativistic dynamical effects in these observables. We plan to explore the cross section out to 750 MeV/c (denoted Q1 and R1 in Table 1) to check if DWIA models [9,20] break down completely at very large $p_{\rm miss}$. In processes where the residual nucleus is left at higher excitation ("high $E_{\rm miss}$"), we propose to measure the cross section, R_{lt}, and A_{lt} out to $E_{\rm miss} \approx 170$ MeV at missing momenta of 70, 140, 210, and 345 MeV/c in order to characterize the longitudinal character of two-nucleon knockout and to look for the predicted two-nucleon correlation ridge, $E_{\rm miss} \approx p_{\rm miss}^2/2m_p$. We note that combining the measurements for these two regions into the same experiment results in substantial savings in the overhead time for setup and calibrations (see 4).

2.1 $1p$*-shell removal*

2.1.1 Theoretical considerations

Very good calculations [9,20] exist now for the removal of protons from the $1p$-shell. The calculation by Udias, in particular, describes our existing ^{16}O$(e,e'p)$ $1p$-shell knockout data out to $p_{\rm miss} = 345$ MeV/c. Since we propose to greatly improve the precision and range of our measurements in order to test aspects of proton knockout, we need to understand the sensitivity of these calculations to their different ingredients. This knowledge lets us plan our measurements for maximum sensitivity to interesting effects. It also will let us know, in the instances when data disagrees with theory, where the theory needs to be improved.

Udias has investigated the sensitivity of his calculations to the choice of bswf and other various ingredients. Details of this investigation can be found in Appendix 3. A summary is presented below.

Relativistic effects - Here we do not refer to relativistic kinematics (which are used in all calculations). Rather, we refer to the inclusion of negative-energy components and spinor distortions in the Dirac formalism [20] or the introduction of spinor distortions by the Effective Momentum Approximation (EMA) in the relativized Schrödinger formalism [9]. Note that the EMA breaks down at $p_{\rm miss} \approx 300$ MeV/c. The $1p$-shell in ^{16}O is very suitable for this study, because the effect of negative energy components is different for the two $1p$-

states, as it is known to be more noticeable for the $l + 1/2$ state than for the $l - 1/2$ state. Our previous results strongly indicate that the R_{lt} and (even more so) A_{lt} observables are very sensitive to the inclusion of these relativistic dynamical effects. The calculations also suggest that this sensitivity is even larger at higher $p_{\rm miss}$ (see Figs. 9 and 10).

Current operator - The sensitivity was tested using two of the most widely used current operators [29]. It is known that $cc2$ tends to minimize the role of the negative-energy components, while $cc1$ over-emphasizes their role. Although our published data prefer the use of $cc2$ over $cc1$, this should be tested over a larger range of $p_{\rm miss}$. Our studies indicate that the sensitivity to the choice of current operator is larger than the sensitivity to the choice of the bswf, if the latter are restricted to the more modern bswf (such as NLSH and NL3).

Optical potential - The sensitivity to several widely used optical potentials of two different classes was tested: a purely phenomenological S-V potential based on the Dirac equation and fitted to energy-dependent elastic scattering data with or without A-dependence, and a potential based on parametrization of N-N data. In general, the sensitivity to the optical potential is very small, especially in R_{lt} and A_{lt}. Our previous data (and other data) are very well-described by the EDAI-O model of the first type. Note that the calculations indicate that the amount of negative-energy components in the wave function is the largest for the calculations using the EDAI-O optical potential.

Gauge prescription - Fully relativistic calculations are less sensitive to gauge prescriptions than non-relativistic ones. Low-$p_{\rm miss}$ data preclude the use of the Weyl gauge. The differences between the Landau and Coulomb gauges are small, especially for the $l - 1/2$ state.

Two-body currents - The calculations by Udias do not include two-body currents, yet their success in predicting our recent data is impressive and suggest that these contributions are small for the published four-momentum transfer range. It is hard to predict reliably the effects of two-body currents, especially at high $p_{\rm miss}$. However, over the previously measured range of $p_{\rm miss}$, the contribution of two-body currents to R_{lt} is estimated to be only 2% (8%) for the $1p_{3/2}$- ($1p_{1/2}$-) states respectively [30]. Additional work on the sensitivity of the calculations to two-body currents is under way.

Channel coupling - Work on the effect of channel coupling is under way.

Contamination of the $1p_{3/2}$*-state* - Contamination of the $1p_{3/2}$ state from the unseparated positive parity $(2s_{1/2}, 1d_{5/2})$ doublet at 17.4 MeV was taken into account in all calculations by including an incoherent contribution due to these states as parametrized by Leuschner [6].

It turns out that A_{lt} is predominantly sensitive to relativistic effects, with much

smaller sensitivities to the usual $(e, e'p)$ ambiguities of the choice of optical potential and gauge. It is also sensitive to the choice of current operator - this is not surprising since this is just another aspect of relativity. Theorists need to treat both the wave function and the current operator properly relativistically.

2.1.2 The proposed 1p-shell measurements

We propose to measure the $1p$-shell $^{16}\mathrm{O}(e, e'p)$ cross section at twenty p_{miss} values ranging from -515 to $+755$ MeV/c (see Table 1) in order to determine

(i) the bound-state wave function and spectroscopic factors for valence knockout;
(ii) the effects of relativity and spinor distortion on valence proton knockout using the diffractive character of the A_{lt} asymmetry; and
(iii) the limits of the validity of the single-particle model of valence proton knockout.

All measurements will be done at $Q^2 = 0.8$ (GeV/c)^2 and $\omega = 0.445$ GeV (quasielastic kinematics), so our data from E89-003 can be added to form a comprehensive data set. We will separate the R_{lt} response and A_{lt} asymmetry for $-515 < p_{\mathrm{miss}} < +515$ MeV/c.

Unfortunately, the eight p_{miss} points from the first part of this experiment were not sufficient to uniquely fix the bswf and the spectroscopic factors independently. In order do this, additional precise measurements over a wide p_{miss} range (but especially at $p_{\mathrm{miss}} < 200$ MeV/c) are needed. We plan to use the roughly 3° angular acceptance of the HRS$_h$ to subdivide the low p_{miss} measurements into overlapping 25 MeV/c bins, allowing us to thoroughly determine both quantities.

Figs. 9 and 10 show the $1p$-shell $^{16}\mathrm{O}(e, e'p)$ longitudinal-transverse interference response R_{lt} and the left-right asymmetry A_{lt} versus missing momentum as measured by E89-003, as calculated by Udias, and as we expect to measure in this proposal. All calculations in Fig. 10 include the contribution of the $(2s_{1/2}, 1d_{5/2})$-doublet. The subscripts '1' and '2' refer to the $cc1$ and $cc2$ in the respective calculation [29]. The 'rel' calculations are fully relativistic. The 'proj' calculations use momentum-dependent projection operators to retain the positive-energy contribution to the spherical wave appearing in the final state due to dispersion by the potentials. This leads to the dispersive effects in the figures. It also results in the differing behavior of A_{lt} and R_{lt} for the two $1p$-shell states at moderate values of p_{miss}. The 'EMA-noSV' calculation uses the Effective Momentum Approximation with only the asymptotic values of the proton momenta and no distortion of the final nucleon spinor. This makes the calculation essentially equivalent to a factorized calculation.

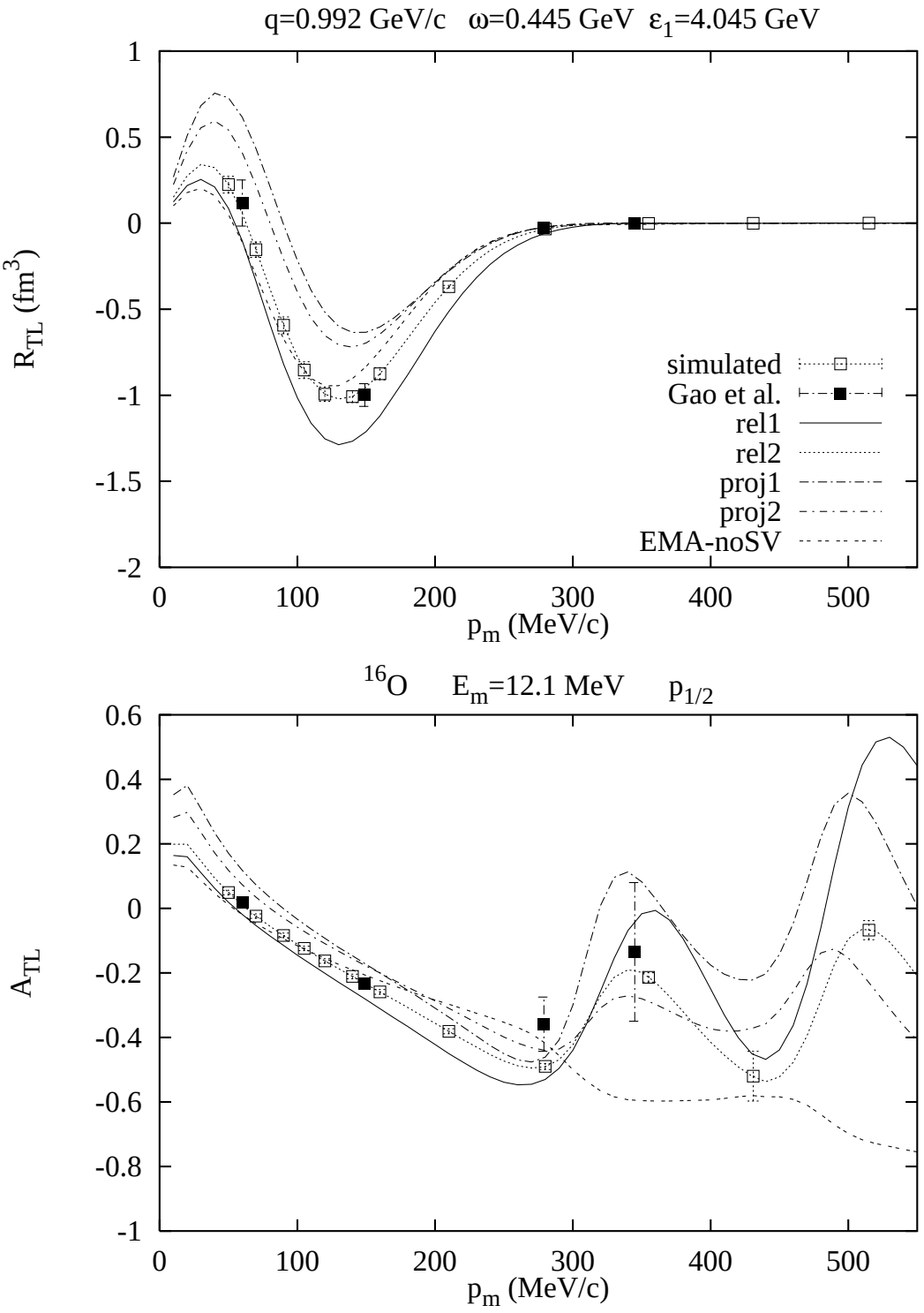

Fig. 9. R_{lt} and A_{lt} for proton knockout from the $1p_{1/2}$-state of ^{16}O as a function of missing momentum. The subscripts '1' and '2' label the use of the $cc1$ and $cc2$ [29] in the respective calculation. The 'rel' calculations are fully relativistic. 'proj' indicates momentum-dependent positive-energy projection operators have been employed. 'EMA' indicates the calculation was performed within the framework of the Effective Momentum Approximation. 'noSV' indicates no spinor distortions are permitted. Figure courtesy J. M. Udias.

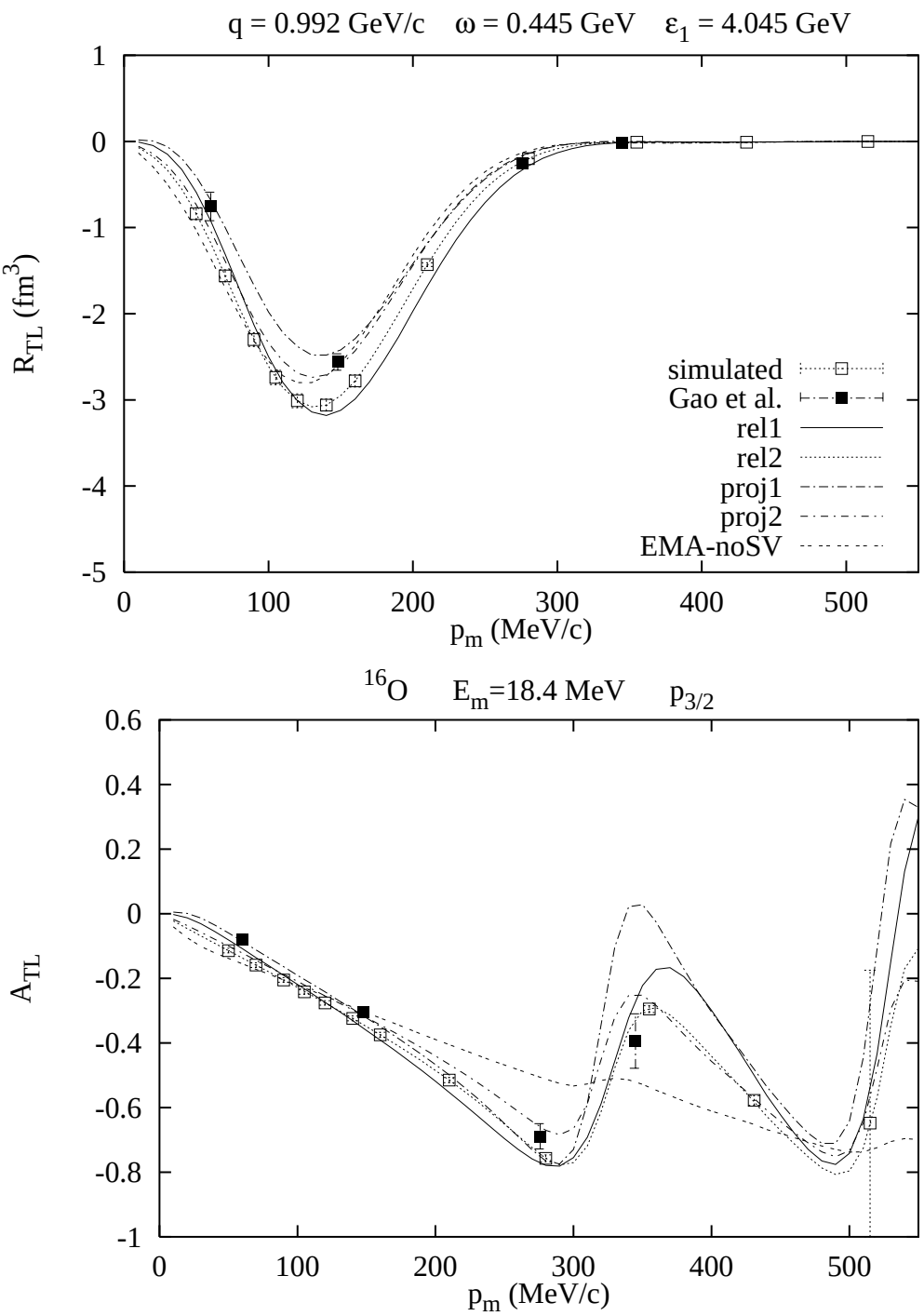

Fig. 10. R_{lt} and A_{lt} for proton knockout from the $1p_{3/2}$-state of ^{16}O as a function of missing momentum. All calculations include the contribution of the $(2s_{1/2}, 1d_{5/2})$-doublet. The subscripts '1' and '2' label the use of the *cc*1 and *cc*2 in the respective calculation [29]. The 'rel' calculations are fully relativistic. 'proj' indicates momentum-dependent positive-energy projection operators have been employed. 'EMA' indicates the calculation was performed within the framework of the Effective Momentum Approximation. 'noSV' indicates no spinor distortions are permitted. Figure courtesy J. M. Udias.

	sensitive range of A_{lt} (MeV/c)	
state	current operator	proper treatment of spinors
$1p_{1/2}$	[0-275], [320-500]	[50-500]
$1p_{3/2}$	[350-450]	[250-400]

Table 2
Sensitive missing momentum range of the observable A_{lt} to the choice of current operator and the proper relativistic treatment of the spinors for the $1p$-shell.

	sensitive range of R_{lt} (MeV/c)	
state	current operator	proper treatment of spinors
$1p_{1/2}$	[100-250]	[0-250]
$1p_{3/2}$	[150-250]	[100-250]

Table 3
Sensitive missing momentum range of the observable R_{lt} to the choice of current operator and the proper relativistic treatment of the spinors for the $1p$-shell.

Note the greatly decreased anticipated error bars and the greatly increased range of missing momentum measured. Note also that the measurements will be in a region of missing momentum where the asymmetry is extremely sensitive to relativistic effects.

Tables 2 and 3 summarize the differential sensitivities of the observables A_{lt} and R_{lt}. In examining the sensitivity to the current operator, we look at the difference between the 'rel1' and 'rel2' calculations. In examining the sensitivity to the proper relativistic treatment of the spinors, we look at the difference between the 'rel2' and 'proj2' calculations.

Clearly, this differential sensitivity to the various aspects of the calculations of the two $1p$-shell states in ^{16}O (as opposed to the single $1p_{3/2}$-state in ^{12}C, for example) is an important degree-of-freedom in this experiment. Examination of the expected error bars indicates that we should easily be able to verify the importance of spinor distortions and to select the appropriate current operator.

At some $p_{\rm miss}$, we expect that two-nucleon effects will become important and the single-nucleon knockout calculations will fail to describe the data. In order to locate this point, we plan to separate R_{lt} and A_{lt} out to $p_{\rm miss} = 515$ MeV/c and to measure the cross section out to 750 MeV/c. Udias is also working on including two-nucleon effects (such as MEC) in his calculations to extend their validity to higher $p_{\rm miss}$.

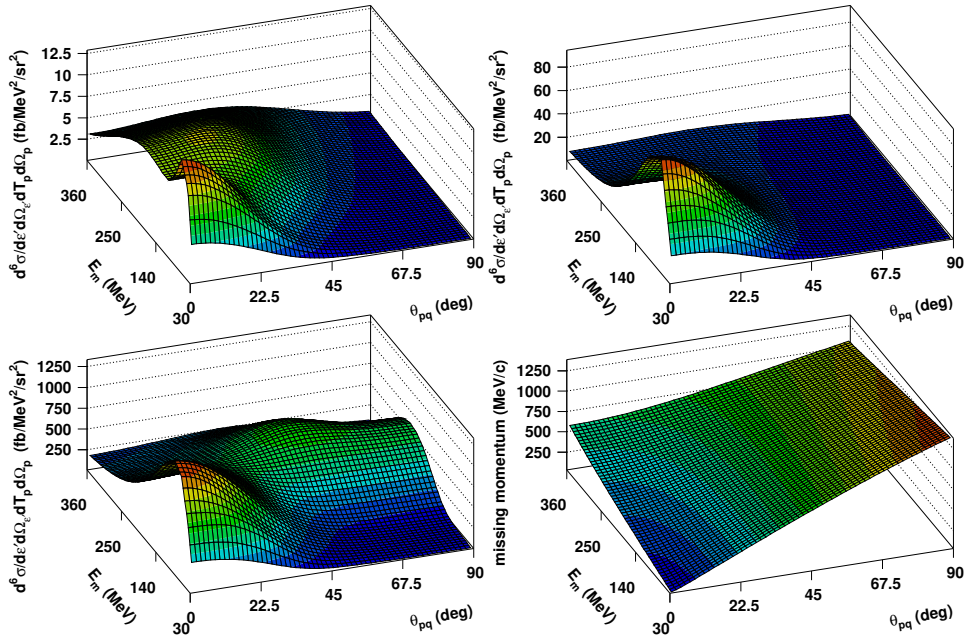

Fig. 11. The calculated contribution from two-nucleon knockout to the differential ^{16}O$(e,e'p)$ cross section versus $E_{\rm miss}$ and θ_{pq} at $E_0 = 2.442$ GeV, $E_f = 1.997$ GeV, and $\theta_e = 23.4°$ ($Q^2 = 0.8$ (GeV/c)^2 and $\omega = 0.445$ GeV) [27]. The upper-left panel includes solely the central correlations, while the upper-right panel has both central and tensor correlations. The lower-left panel includes central and tensor correlations (two-nucleon correlations) plus Meson Exchange Currents and Isobar Currents (two-body currents). The lower-right panel shows the variation of the $p_{\rm miss}$ as a function of $E_{\rm miss}$ and θ_{pq}. Figure courtesy J. Ryckebusch.

2.2 $1s_{1/2}$-state and higher missing energies

2.2.1 Theoretical considerations

The same calculations [9,20] which nicely reproduce the characteristics of $1p$-shell removal fail to describe not only the experimentally observed features of the $1s_{1/2}$-state removal, but also those for the higher missing energies [18]. This failure increases with increasing missing momentum. This is not surprising, since the $1s_{1/2}$-state peak at $E_{\rm miss} \approx 40$ MeV is only apparent at low missing momentum. At higher missing momentum, the single-nucleon knockout peak is masked by more complicated structures and processes.

At larger missing energy, $80 < E_{\rm miss} < 120$ MeV, the cross section is almost constant as a function of both missing energy and missing momentum. Unfactorized $(e,e'pp)$ and $(e,e'pn)$ knockout calculations by Ryckebusch [27], which include two-body currents and N-N short-range (Jastrow) and tensor correla-

tions, reproduce this constant behavior and underestimate the cross section by only a factor of two [18]. All three elements (central and tensor correlations and two-body currents) are necessary to reproduce the large observed cross section. The three elements also have varying importance in different parts of the $(E_{\rm miss}, \theta_{pq})$ plane. This calculation also predicts the existence of the 'two-nucleon correlation ridge' where $E_{\rm miss} \approx p^2_{\rm miss}/2m_p$.

2.2.2 The proposed $1s_{1/2}$-state measurements

To further understand the reaction at $E_{\rm miss} > 20$ MeV, a region that includes the $1s_{1/2}$-state, we propose to measure the cross section, R_{lt} response, and A_{lt} asymmetry as a function of missing energy ($0 < E_{\rm miss} < 160$ MeV) for missing momenta centered at $\pm$70, $\pm$140, $\pm$210, and $\pm$345 MeV/c. This will help us to determine whether or not these cross sections are due to two-body currents which are mainly transverse in nature, or to initial-state correlations (Jastrow), which are predominantly longitudinal. We expect the nature of the observed strength to change as a function of missing momentum. In particular, the ridge defined by $E_{\rm miss} \approx p^2_{\rm miss}/2m_p$ should be different for low $p_{\rm miss}$ than for $p_{\rm miss}$ above the Fermi-momentum, where it is expected to be due to short-range N-N correlations.

We also hope to use R_{lt} and A_{lt} to disentangle the predominantly transverse two-body currents (such as MEC and IC) from the two-nucleon correlations (central and tensor). R_{lt} should be very different in a region where two-nucleon correlations are large than in a region where they are small. This is true even in a region where we expect the two-body currents to be much larger than two-nucleon correlations (see Fig. 11).

Again, the details of the proposed kinematics are presented in Table 1. Note that the measurements at the higher $E_{\rm miss}$ entail only lowering the magnetic field settings of the HRS$_h$ spectrometer, and hence there is essentially no additional experimental overhead. Moreover, the monitoring of the luminosity does not change, as the both the HRS$_e$ field and angle settings stay fixed. Hence, there are no additional or separate systematic uncertainties incurred by this part of the measurement.

3 Simulations and rate estimates

3.1 Overview

The following sections summarize the experiment simulations performed using the latest version of the code `MCEEP` [31]. A complete archive of the simulations may be found at [32].

3.2 Phase space

Phase space simulations were performed to determine the field settings to be used for the HRS_h, as well as the acceptance overlap between the various proposed kinematical points.

3.2.1 Acceptance matching

At a field excitation of 3.600 GeV/c, the HRS_e has a very large acceptance in both energy and momentum transfer (ω,q). Since a structure function separation requires the matching of the four variables (ω,q,E_{miss},p_{miss}), we studied the effect this large (ω,q)-acceptance had on the entire experimental phase space at each of the kinematics. The following plot shows a representative portion of the results of this study for the proposed F1 and K1 kinematics.

Consider the entire (ω,q)-acceptance of the HRS_e illustrated in the upper left-hand corner of Fig. 12. The corresponding (E_{miss},p_{miss}) acceptance of the HRS^2 is shown in the bottom left-hand corner. We divided this acceptance into four smaller bins, each about 50 MeV $\times$ 50 MeV/c, with one bin in each of the corners of the full acceptance parallelogram (see the plot in the upper right-hand corner which shows one of these bins). The effect this cut has on the (E_{miss},p_{miss})-acceptance is shown in the bottom right-hand corner.

Clearly, events sampled from the extreme regions of the (ω,q)-acceptance have a rather poor (E_{miss},p_{miss}) overlap. Thus, to ensure excellent overlap in our data, we have enforced a 50 MeV $\times$ 50 MeV/c central (ω,q) cut upon our simulations (see Fig. 13). The implications of this cut on our rate estimates are discussed in 3.3.

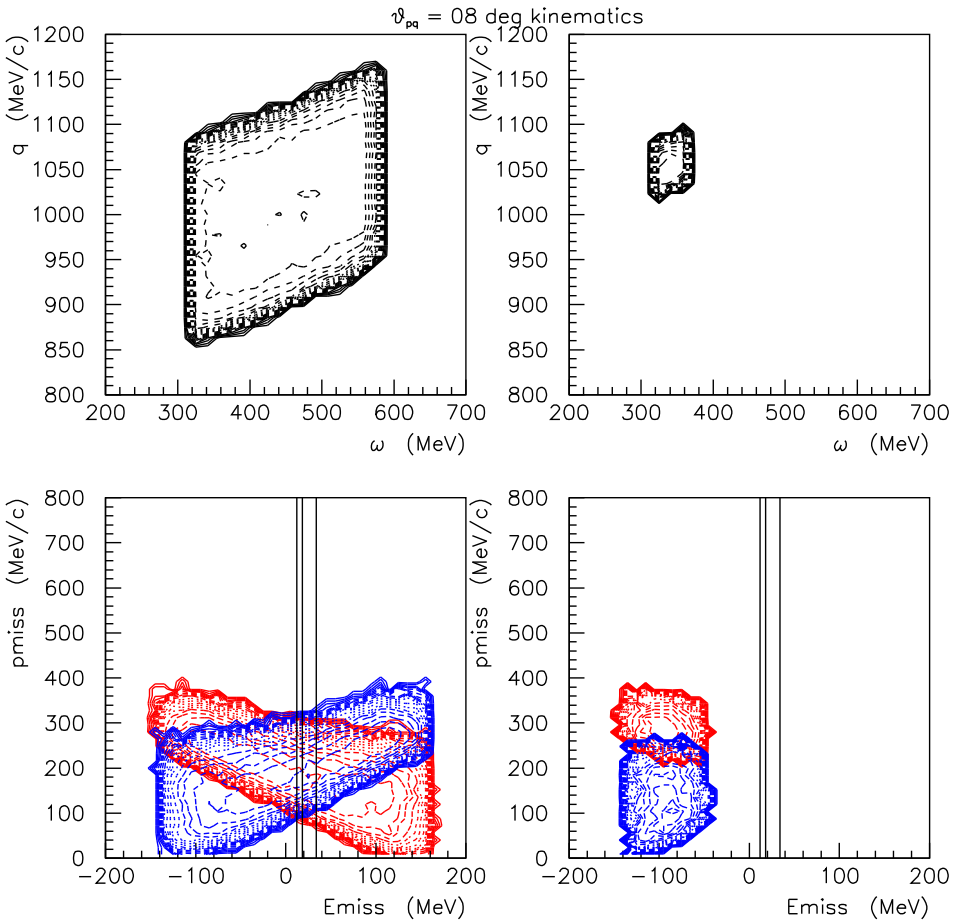

Fig. 12. The effect of a low-ω, high-q cut on the F1/K1 ($E_{\rm miss}$,$p_{\rm miss}$) overlap. The three vertical lines represent the $E_{\rm miss}$ position of the $1p_{1/2}$-, $1p_{3/2}$-, and $1s_{1/2}$-states (from left to right).

3.2.2 Missing energy acceptance

In order to perform the proposed A_{lt} and R_{lt} separations at higher missing energies, we have carefully matched not only the absolute (ω,q,$E_{\rm miss}$,$p_{\rm miss}$) acceptances for each contributing kinematical point, but also the relative (ω,q,$E_{\rm miss}$,$p_{\rm miss}$) acceptances between each successive HRS$_h$ momentum bite (see Fig. 14).

This is very important as it will allow us to systematically and rigorously tie the measurements for the three different momentum bites together in a smooth and continuous fashion, essentially normalizing the deep-continuum measurement to the bound-state measurement via an intermediate measurement at each kinematics.

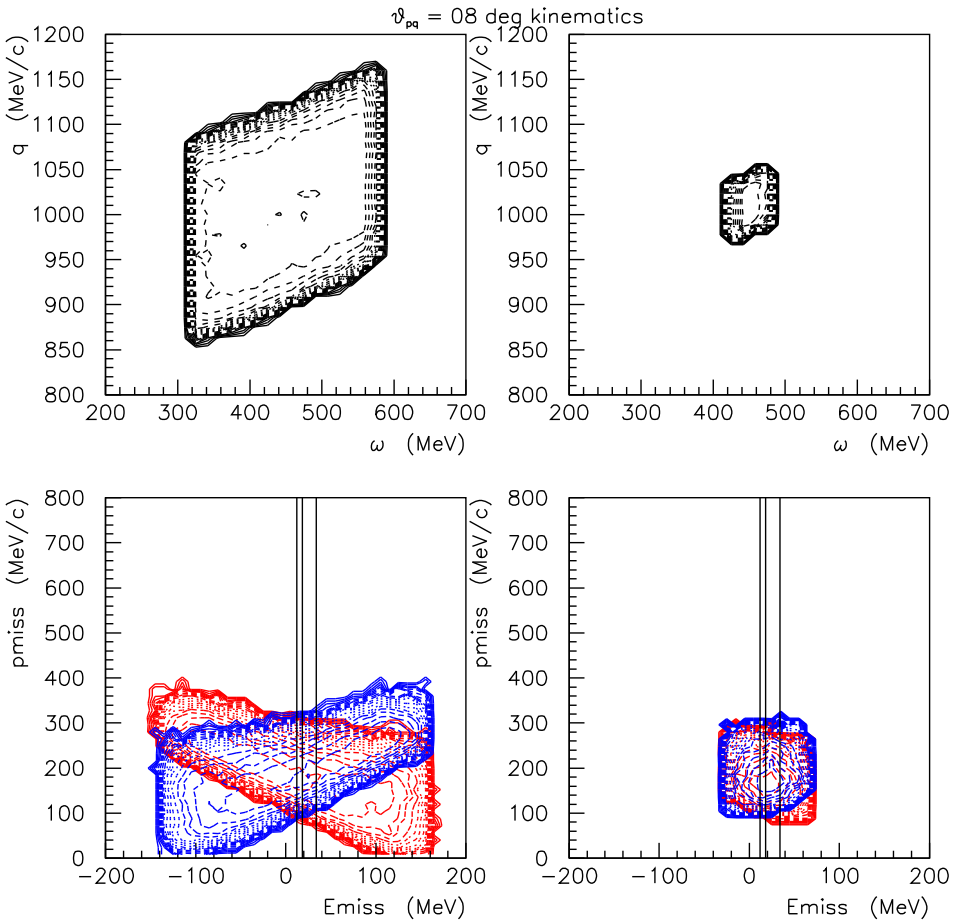

Fig. 13. The effect of a central (ω,q) cut on the F1/K1 ($E_{\rm miss}$,$p_{\rm miss}$) overlap. The three vertical lines represent the $E_{\rm miss}$ position of the $1p_{1/2}$-, $1p_{3/2}$-, and $1s_{1/2}$-states (from left to right).

3.3 Coincidence cross sections and rates

The input parameters were

(i) target: three 250 mg/cm^2 foils of H_2O oriented such that the perpendicular to the surface of the foil made an angle of 30° with respect to the incident electron beam direction.
(ii) beam current: 100 μA, resulting in a luminosity of 77.0 μA·g/cm^2 for ^{16}O and 9.6 μA·g/cm^2 for ^{1}H.
(iii) physics "models":
  (a) bound states - the calculations of Udias [20] (with spectroscopic factors of 0.7) which do an excellent job of representing the data of Gao *et al.* [10]; and
  (b) continuum - the data of Liyanage *et al.* [18].
(iv) coincidence time-of-flight peak width: 1 ns.
(v) spectrometer models - on, radiative effects - off, energy loss - off.

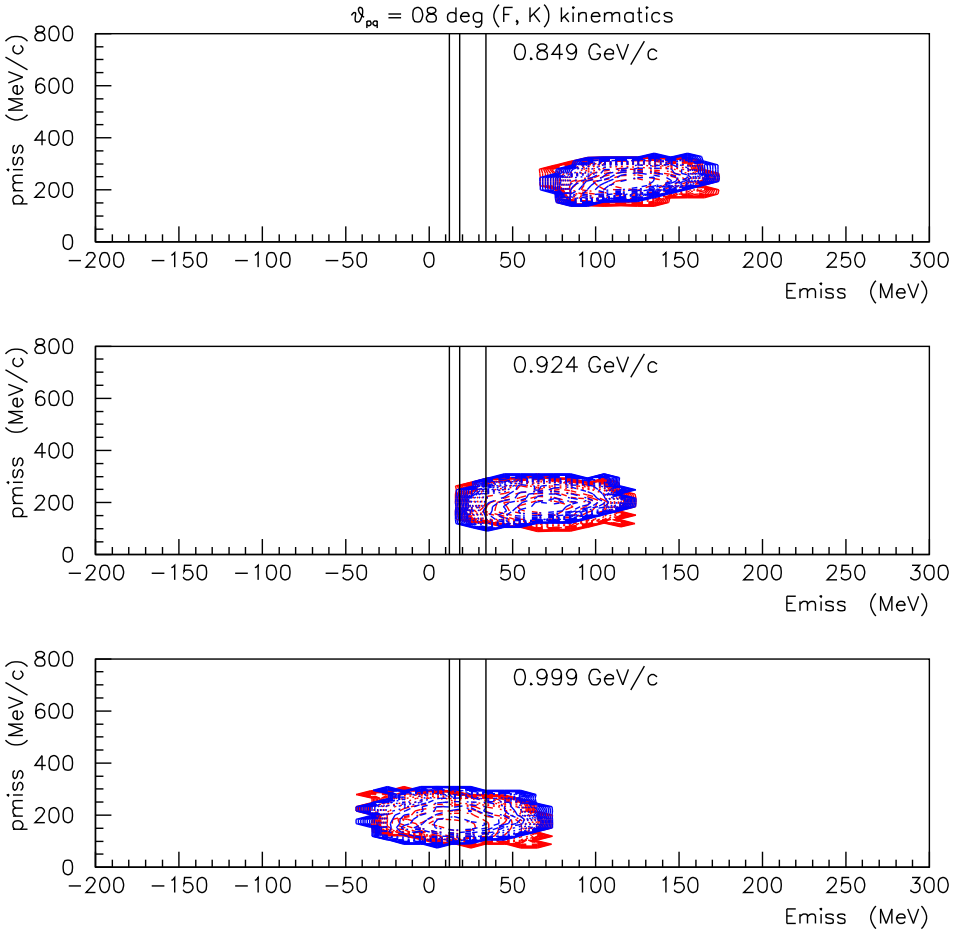

Fig. 14. An illustration of the relative (ω,q,$E_{\rm miss}$,$p_{\rm miss}$) acceptance overlap between successive HRS$_h$ momentum bites.

Note that in all cases, we quote rates for a central 50 MeV × 50 MeV/c ωq-bin. The full ωq-acceptance is approximately 12× larger.

3.3.1 Lowest missing energy ('kinematics 1')

For the 'kinematics 1' measurements, the central momentum of the HRS$_h$ is set so that the $1p$-shell and $1s_{1/2}$-state are within the coincidence acceptance of the HRS[2]. Table 4 summarizes the anticipated cross sections and rates for a central 50 MeV × 50 MeV/c ωq-bin. Note that the anticipated values for kinematics Q1 and R1 are for the full spectrometer acceptances since no structure function separation will be performed using this data and thus no phase space matching is necessary. Also note that the $1s_{1/2}$-state cross sections and rates for $p_{\rm miss} > 150$ MeV/c are dominated by the flat continuum (see 3.3.2).

	Udias $d^5\sigma$ (pb/MeV/sr^2)			rate (/hour)		
label	$1p_{1/2}$	$1p_{3/2}$	$1s_{1/2}$	$1p_{1/2}$	$1p_{3/2}$	$1s_{1/2}$
A1	0.294	0.176	0.265	47.5	3.3	2.6
B1	0.814	4.216	0.160	20.6	128.3	2.3
C1	6.799	14.550	4.974	128.6	206.9	31.3
D1	27.660	44.780	10.980	440.8	590.1	74.2
E1	489.900	1062.000	111.100	7464.1	14478.0	731.5
F1	3173.000	5519.000	1723.000	47102.0	83526.0	10901.0
G1	5100.000	7731.000	4265.000	82110.0	133090.0	27716.0
H1	5355.000	7109.000	8230.000	105010.0	168150.0	54173.0
I1	5605.000	9747.000	12020.000	108160.0	192190.0	96444.0
J1	6573.000	12630.000	7685.000	100430.0	203360.0	64946.0
K1	4912.000	10910.000	3954.000	69289.0	157930.0	35016.0
L1	1113.000	3453.000	497.200	14485.0	47323.0	4822.7
M1	81.890	363.900	18.710	997.5	4839.9	190.1
N1	9.807	17.750	9.401	112.1	221.2	99.5
O1	2.489	1.116	1.345	263.4	173.1	18.0
P1	0.335	0.839	0.210	9.9	14.5	2.6
Q1	0.077	0.225	0.026	6.6	2.1	2.3
R1	0.008	0.009	0.006	0.5	0.7	0.5

Table 4
Anticipated cross sections and rates for 'kinematics 1' (the $1p$-shell and the $1s_{1/2}$-state) for a central 50 MeV $\times$ 50 MeV/c ωq-bin for every kinematics except Q1 and R1, whose values are quoted for the full spectrometer acceptances. The $1s_{1/2}$-state cross sections and rates for $p_{\rm miss} > 150$ MeV/c are dominated by the flat continuum (see 3.3.2).

3.3.2 Moderate missing energy ('kinematics 2')

For the 'kinematics 2' measurements, the central momentum of the HRS$_h$ is set so that the $1s_{1/2}$-state and the shallow continuum are within the coincidence acceptance of the HRS^2. Table 5 (6) summarizes the anticipated cross sections and rates for a central 50 MeV $\times$ 50 MeV/c ωq-bin for the $1s_{1/2}$-state (shallow continuum). For $p_{\rm miss} > 150$ MeV/c, they are dominated by the flat continuum (see Table 6).

label	Udias $d^5\sigma$ (pb/MeV/sr^2)	rate (/hour)
C2	4.9	64.2
E2	111.1	800.1
F2	1723.0	11191.0
H2	8230.0	48023.0
I2	12020.0	55065.0
K2	3954.0	15252.0
L2	497.2	1543.1
N2	9.4	12.7

Table 5
Anticipated cross sections and rates for the $1s_{1/2}$-state for HRS$_h$ momentum bite 2. A central 50 MeV $\times$ 50 MeV/c ωq-bin is considered. For $p_{\rm miss} > 150$ MeV/c, they are dominated by the flat continuum (see Table 6).

label	Liyanage $d^6\sigma$ (pb/(MeV)^2/sr^2)	$\int_{60}^{110} d^6\sigma\ dE_{miss}$ = Liyanage $d^5\sigma$ (pb/MeV/sr^2)	rate (/hour/bin)
C2	2.0	100.0	2650
E2	18.0	900.0	23846
F2	10.0	500.0	11658
H2	5.0	250.0	6624
I2	5.0	250.0	6624
K2	10.0	500.0	11658
L2	18.0	900.0	23846
N2	2.0	100.0	2650

Table 6
Anticipated cross sections and rates for the shallow continuum for HRS$_h$ momentum bite 2. A central 50 MeV $\times$ 50 MeV/c ωq-bin is considered. We gain a factor of 2.3 in rate due to the increase in $\sigma_{\rm Mott}$ which is included in the quoted value. We assume a bin width of 5 MeV in missing energy in the rate column.

3.3.3 Largest missing energy ('kinematics 3')

For the 'kinematics 3' measurements, the central momentum of the HRS$_h$ is set so that moderate-to-deep continuum is within the coincidence acceptance of the HRS[2]. Table 7 summarizes the anticipated cross sections and rates for a central 50 MeV $\times$ 50 MeV/c ωq-bin.

label	Liyanage $d^6\sigma$ (pb/(MeV)^2/sr^2)	$\int_{70}^{150} d^6\sigma\ dE_{miss}$ = Liyanage $d^5\sigma$ (pb/MeV/sr^2)	rate (/hour/bin)
C3	2.0	160.0	2650
E3	18.0	1440.0	23846
F3	10.0	800.0	11658
H3	5.0	400.0	6624
I3	5.0	400.0	6624
K3	10.0	800.0	11658
L3	18.0	1440.0	23846
N3	2.0	160.0	2650

Table 7
Anticipated cross sections and rates for the moderate-to-deep continuum for HRS_h momentum bite 3. A central 50 MeV $\times$ 50 MeV/c ωq-bin is considered. We gain a factor of 2.3 in rate due to the increase in $\sigma_{\rm Mott}$ which is included in the quoted value. We assume a bin width of 5 MeV in missing energy in the rate column.

3.4 Background

Backgrounds were modeled to check for possible problems with $\pi^{\pm}$ contamination of the data, to determine the anticipated signal-to-noise ratios for the $1p$-shell of ^{16}O, and to check for contamination of the data from elastic electron scattering from ^{1}H in the vicinity of q.

3.4.1 ^{16}O

Singles rates for the (e,e'), (e,π^-), (e,p), and (e,π^+) backgrounds from ^{16}O were extracted using the routines of Lightbody and O'Connell [33] as incorporated into `MCEEP`. They are presented in Table 8, while the corresponding hourly accidental rates per MeV of $E_{\rm miss}$ are presented in Table 9.

label	(e,e') ($\times 10^8$/hour)	(e,π^-) ($\times 10^7$/hour)	(e,p) ($\times 10^8$/hour)	(e,π^+) ($\times 10^7$/hour)
A1	4.12	3.28	4.78	6.55
B1	4.12	3.28	4.29	6.29
C1	4.12	3.28	3.85	6.04
C2	4.12	3.28	4.09	6.02
C3	4.12	3.28	4.46	6.01
D1	4.12	3.28	3.49	5.81
E1	4.12	3.28	3.12	5.58
E2	4.12	3.28	3.31	5.57
E3	4.12	3.28	3.64	5.56
F1	4.12	3.28	2.73	5.35
F2	4.12	3.28	2.94	5.34
F3	4.12	3.28	3.24	5.34
G1	4.12	3.28	2.52	5.22
H1	4.12	3.28	2.32	5.10
H2	4.12	3.28	2.54	5.10
H3	4.12	3.28	2.84	5.10
I1	4.12	3.28	0.50	4.62
I2	4.12	3.28	1.46	4.64
I3	4.12	3.28	1.37	4.86
J1	4.12	3.28	0.25	4.46
K1	4.12	3.28	0.23	4.32
K2	4.12	3.28	0.31	4.36
K3	4.12	3.28	0.51	4.39
L1	4.12	3.28	0.20	3.95
L2	4.12	3.28	0.27	4.09
L3	4.12	3.28	0.41	4.14
M1	4.12	3.28	0.17	1.36
N1	4.12	3.28	0.14	-
N2	4.12	3.28	0.20	1.77
N3	4.12	3.28	0.28	3.59
O1	4.12	3.28	0.11	-
P1	4.12	3.28	0.09	-
Q1	4.12	3.28	0.06	-
R1	4.12	3.28	0.04	-

Table 8
Hourly background (singles) rates from ^{16}O. A $\pi^{\pm}$ suppression factor of 1000 is anticipated [34] but not included in the above numbers. The π^+ calculation is unreliable for kinematics N1, O1 - R1.

label	$(e, e'p)$ (/hour)	$(e, e'\pi^+)$ (/hour)	$(e, \pi^- p)$ (/hour)	$(e, \pi^-\pi^+)$ (/hour)
A1	188.82	25.89	15.02	2.06
B1	169.62	24.84	13.50	1.97
C1	152.07	23.85	12.10	1.89
C2	161.42	23.79	12.84	1.89
C3	176.34	23.75	14.03	1.89
D1	137.98	22.97	10.98	1.82
E1	123.25	22.05	9.81	1.75
E2	130.97	22.01	10.42	1.75
E3	143.90	21.98	11.45	1.75
F1	107.69	21.13	8.57	1.68
F2	115.96	21.11	9.23	1.68
F3	128.08	21.09	10.19	1.67
G1	99.69	20.63	7.93	1.64
H1	91.53	20.14	7.28	1.60
H2	100.42	20.15	7.99	1.60
H3	112.10	20.15	8.92	1.60
I1	19.72	18.25	1.56	1.45
I2	57.81	18.32	4.60	1.45
I3	54.06	19.20	4.30	1.52
J1	9.97	17.62	0.79	1.40
K1	9.18	17.07	0.73	1.35
K2	12.48	17.23	0.99	1.37
K3	20.24	17.36	1.61	1.38
L1	7.88	15.59	0.62	1.24
L2	10.55	16.15	0.84	1.28
L3	16.47	16.35	1.31	1.30
M1	6.67	5.38	0.53	0.42
N1	5.59	-	0.44	-
N2	7.76	6.98	0.61	0.55
N3	11.11	14.19	0.88	1.12
O1	4.46	-	0.35	-
P1	3.54	-	0.28	-
Q1	2.42	-	0.19	-
R1	1.69	-	0.13	-

Table 9
Hourly background (singles) rates from ^{16}O per MeV of $E_{\rm miss}$. A $\pi^{\pm}$ suppression factor of 1000 is anticipated [34] but not included in the above numbers. The π^+ calculation is unreliable for kinematics N1, O1 - R1.

Table 9 presents the hourly background (singles) rates from ^{16}O per MeV of $E_{\rm miss}$. A base-width coincidence time-of-flight peak of 1 ns was assumed in calculating these numbers. Given the anticipated $\pi^{\pm}$ suppression factor of 1000 [34], we conclude the only background of significance from ^{16}O is from $(e, e'p)$ accidentals.

Table 10 presents the anticipated signal-to-noise ratios for the $1p$-shell of ^{16}O for the various kinematics. The signal input comes from Table 4, while the noise input comes from Table 9. In calculating these numbers, a timing resolution of 1 ns and a missing energy base-width of 1.8 MeV was chosen for both the $1p$-shell states.

Note that the signal-to-noise ratio (R) drops significantly below unity for kinematics A, B, C, and R. This causes two problems:

(i) locating the time-of-flight peak; and
(ii) decreasing the statistical accuracy of the measurement.

We will be able to locate the TOF peak since the continuum ($E_{\rm miss} > 25$ MeV) cross section should be much larger than the $1p$-shell knockout cross section. The relative statistical uncertainty will increase by a factor of $\sqrt{1 + 1/R}$ from $\sqrt{1/N}$ to $\sqrt{(1 + 1/R)/N}$ where N is the number of counts due to true coincidences. We have taken this factor into account in our projected uncertainties (recall Figs. 9 and 10).

label	$1p_{1/2}$	$1p_{3/2}$
A1	0.14	0.01
B1	0.07	0.42
C1	0.47	0.76
D1	1.77	2.38
E1	33.64	65.26
F1	242.99	430.90
G1	457.59	741.70
H1	637.31	1020.51
I1	3047.62	5415.33
J1	5594.99	11329.25
K1	4191.71	9554.14
L1	1020.79	3334.95
M1	83.06	402.99
N1	11.14	21.99
O1	32.80	21.56
P1	1.55	2.27
Q1	1.52	0.48
R1	0.16	0.23

Table 10
Anticipated signal-to-noise ratio R for the $1p$-shell of ^{16}O. A base-width of 1.8 MeV was chosen for the $1p$-shell states. Recall that while kinematics Q1 and R1 are measured for the full HRS^2 acceptance, all other kinematics consider only a central 50 MeV $\times$ 50 MeV/c ωq-bin.

3.4.2 ^{1}H

Hydrogen singles rates were also calculated using `MCEEP`. They are small. The electron rates are roughly 30% of the $^{16}\mathrm{O}(e,e'p)$ rate. The $^1\mathrm{H}(e,e'p)$ rate (including the effects of radiative tail) is non-negligible only in the vicinity of q, where it will be removed by kinematical cuts.

4 Beam time request

Table 11 summarizes our beamtime request for each kinematics, and includes our best estimate of the statistical accuracy we will obtain with each measurement for the indicated region of E_{miss}. Measurements with high statistical accuracy will be subdivided into smaller bins in missing momentum.

label	$< p_{\rm miss} >$ (GeV/c)	time (hr)	$1p_{1/2}$	$1p_{3/2}$	$1s_{1/2}$	[60-110] MeV (/bin)	[70-150] MeV (/bin)
A1	-0.515	96	4560	312	247	-	-
B1	-0.431	72	1483	9238	166	-	-
C1	-0.346	48	6173	9931	1504	-	-
C2	-0.343	8	-	-	514	21200	-
C3	-0.355	8	-	-	-	-	21200
D1	-0.278	24	10579	14162	1782	-	-
E1	-0.209	4	179138	57912	2926	-	-
E2	-0.215	8	-	-	6401	190768	-
E3	-0.246	8	-	-	-	-	190768
F1	-0.140	4	188408	334104	43604	-	-
F2	-0.155	8	-	-	89528	93264	-
F3	-0.199	8	-	-	-	-	93264
G1	-0.105	4	328440	532360	110864	-	-
H1	-0.070	4	420040	672600	216692	-	-
H2	-0.101	8	-	-	384184	52992	-
H3	-0.163	8	-	-	-	-	52992
I1	+0.070	4	432640	768760	385776	-	-
I2	+0.101	8	-	-	440520	52992	-
I3	+0.163	8	-	-	-	-	52992
J1	+0.105	4	401840	813440	259784	-	-
K1	+0.140	4	277156	631720	140064	-	-
K2	+0.155	8	-	-	122016	93264	-
K3	+0.199	8	-	-	-	-	93264
L1	+0.209	4	570940	189292	19291	-	-
L2	+0.215	8	-	-	12345	190768	-
L3	+0.246	8	-	-	-	-	190768
M1	+0.278	24	23940	116158	4562	-	-
N1	+0.346	48	5381	10618	4774	-	-
N2	+0.343	8	-	-	102	21200	-
N3	+0.355	8	-	-	-	-	21200
O1	+0.431	72	18965	12463	1295	-	-
P1	+0.515	96	950	1392	252	-	-
Q1	+0.644	24	158	50	55	-	-
R1	+0.755	24	12	17	11	-	-

Table 11
The total beamtime request for each kinematics, including an estimate of the total number of counts to be obtained for the indicated $E_{\rm miss}$ region. We assume a bin width of 5 MeV in $E_{\rm miss}$ in the continuum, and 100% efficient data-taking hours.

5 Summary

5.1 Our physics goals

This proposed series of measurements will allow us to take advantage of the unprecedented combination of precision experimental apparatus, superb relativistic $(e, e'p)$ DWIA calculations, and observables sensitive to specific parameters to

(i) determine bound state wave functions and spectroscopic factors at high momentum transfer;
(ii) determine the effects of relativity and spinor distortion on valence proton knockout;
(iii) determine the limits of validity of the single-particle model of valence proton knockout (something that can only be done when an accurate theory exists); and
(iv) study the character of two-nucleon knockout at high missing energies, in an attempt to disentangle two-body currents from two-nucleon correlations.

5.2 Our beamtime request

Our total beamtime request may be broken down in the manner illustrated in Table 12.

purpose	time (hr)	time (days)
valence $1p$-shell lt-separation	512	21.33
high $E_{\rm miss}$ (continuum) lt-separation	128	5.33
very high $p_{\rm miss}$ valence $1p$-shell exploration	48	2.00
normalizations, calibrations, and configuration changes	48	2.00

Table 12
Breakdown of the total beamtime request. Each hour of beamtime is assumed to be 100% efficient at a beam current of 100 μA.

The total is 736 hours (30.67 days). We assume 100% efficient data-taking taking at a beam current of 100 μA.

Acknowledgement

We wish to acknowledge the invaluable contributions and theoretical guidance of J. J. Kelly, J. Ryckebusch, and J. M. Udias in the generation of this proposal.

References

[1] H. Müther *et al.*, Phys. Rev. **C49**, R17 (1994).

[2] F. Garibaldi *et al.*, Nucl. Instrum. Methods **A314**, 1 (1992).

[3] M. Bernheim *et al.*, Nucl. Phys. **A375**, 381 (1982).

[4] L. Chinitz *et al.*, Phys. Rev. Lett. **67**, 568 (1991).

[5] C. M. Spaltro *et al.*, Phys. Rev. **C48**, 2385 (1993).

[6] M. Leuschner *et al.*, Phys. Rev **C49**, 955 (1994).

[7] K. I. Blomqvist *et al.*, Phys. Lett. **B344**, 85 (1995).

[8] J. J. Kelly, Adv. Nucl. Phys. **23**, 75 (1996); Phys. Rev. **C56**, 2672 (1997).

[9] J. J. Kelly, Phys. Rev. **C60**, 044609 (1999).

[10] J. Gao *et al.*, Phys. Rev. Lett. **84**, 3265 (2000).

[11] P. E. Ulmer *et al.*, Phys. Rev. Lett. **59**, 2259 (1987).

[12] G. van der Steenhoven *et al.*, Nucl. Phys. **A480**, 547 (1988).

[13] J. B. J. M. Lanen *et al.*, Phys. Rev. Lett. **64**, 2250 (1990).

[14] D. Dutta, Ph.D. thesis, Northwestern University, 1999 (unpublished).

[15] T. Takaki, Phys. Rev. **C39**, 359 (1989).

[16] J. Ryckebusch *et al.*, Nucl. Phys. **A624**, 581 (1997).

[17] A. Gil *et al.*, Nucl. Phys. **A627**, 599 (1997).

[18] N. Liyanage *et al.*, to be submitted to Phys. Rev. Lett. in 2000.

[19] A. Saha, W. Bertozzi, R. W. Lourie, and L. B. Weinstein, JLAB proposal 89-003, 1989; see also K.G. Fissum, MIT-LNS Internal Report #02, 1997 and `http://www.jlab.org/~fissum/e89003.html`

[20] J. M. Udias *et al.*, Phys. Rev. Lett. **83**, 5451 (1999).

[21] M. M. Sharma, M. A. Nagarajan, and P. Ring, Phys. Lett. **B312**, 377 (1993).

[22] L. Lapikas *et al.*, LANL preprint nucl-ex/9905009 v2 (2000).

[23] J. M. Udias, private communication.

[24] J. Ryckebusch *et al.*, Nucl. Phys. **A476**, 237 (1988).

[25] J. Ryckebusch *et al.*, Nucl. Phys. **A503**, 694 (1989).

[26] V. Van der Sluys *et al.*, Phys. Rev. **C55**, 1982 (1997).

[27] S. Janssen *et al.*, Nucl. Phys. **A672**, 285 (2000).

[28] J.P. Jeukenne and C. Mahaux, Nucl. Phys. **A394**, 445 (1983).

[29] T. de Forest Jr., Nucl. Phys. **A392**, 232 (1983).

[30] J. E. Amaro, private communications.

[31] `http://www.physics.odu.edu/~ulmer/mceep/mceep.html`

[32] `http://www.jlab.org/~fissum/e89003/e89003b.html`

[33] J. W. Lightbody and J. S. O'Connell, *Computers in Physics*, May/June 1988, p. 57.

[34] B. Wojtsekhowski, private communication.

Appendix 1

J. Gao *et al.*, Phys. Rev. Lett. **84**, 3265 (2000).

Appendix 2

N. Liyanage *et al.*, to be submitted to Phys. Rev. Lett. in 2000.

Appendix 3

J. M. Udias, private communication.